

Synergized Cu/Pb Core/Shell Electrocatalyst for High-Efficiency CO₂ Reduction to C₂₊ Liquids

Pengtang Wang,[#] Hao Yang,[#] Yong Xu,[#] Xiaoqing Huang,^{*} Juan Wang, Miao Zhong, Tao Cheng, and Qi Shao^{*}



Cite This: *ACS Nano* 2021, 15, 1039–1047



Read Online

ACCESS |

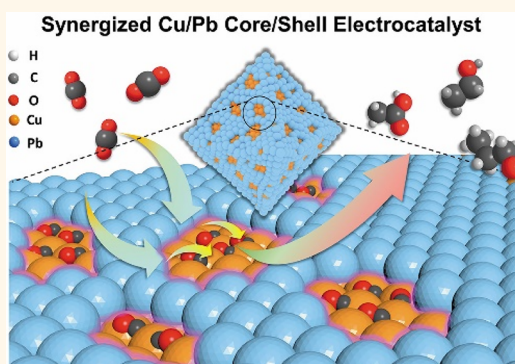
Metrics & More

Article Recommendations

Supporting Information

ABSTRACT: The design of efficient copper-based (Cu-based) carbon dioxide reduction (CO₂RR) electrocatalysts is crucial for converting CO₂ to value-added liquid products. In this work, we demonstrate that the strong synergy between Cu core and ultrathin lead (Pb) shell (0.7 nm) in the Cu/Pb core/shell nanocrystals (NCs, CuPb-0.7/C) significantly boosts the electrocatalytic reduction of CO₂ toward C₂₊ products (products with at least two carbon atoms). Specifically, when applying in a flow cell system, the Faradaic efficiency (FE) of total C₂₊ products and the selectivity of C₂₊ liquid products are as high as 81.6% and 49.5%, respectively. Moreover, the current density of C₂₊ liquid products reaches 196.8 mA cm⁻², outperforming most of the reported Cu-based catalysts for CO₂RR toward the production of C₂₊ liquid products. Density functional theory calculations indicate that the synergized Cu/Pb core/shell NCs reduce the formation energies of *COOH and *OCCOH intermediates, as the two critical intermediates for the reduction of CO₂ to CO and the formation of C₂₊ products, respectively, and leads to the significant increase in the selectivity of C₂₊ liquid products. This study provides an efficient Cu-based catalyst for the reduction of CO₂, highlighting the importance of synergistic effect for the design of electrocatalysts in catalysis.

KEYWORDS: copper, lead, core–shell, synergy, CO₂ reduction reaction



The electrocatalytic reduction of CO₂ (CO₂RR) has been regarded as an imperative technology in this century because it is a promising method for converting electricity from renewable resources into value-added chemicals and thus reducing the emission of CO₂ in industry.^{1–4} Among those different products of CO₂RR, C₂₊ liquid products have attracted the attention of scientists owing to their advantages of high-energy-density, long-term, large-scalable energy storage as well as convenient transportation.^{5–8} Many studies revealed that Au-, Zn-, Sn-, and Pb-based catalysts can only favored the formation of C₁ products (products with only one carbon atom) for CO₂RR.^{9–14} In a sharp contrast, Cu is the only element that can couple two *CO intermediates to form C₂₊ products (products with at least two carbon atoms).^{15–19} Despite the significant progress in this field, it is still greatly challenging to regulate the high selectivity of C₂₊ liquid products for CO₂RR,^{5–7} highly requiring the rational design of efficient catalysts.^{20–27}

The development of multicomposite catalysts has attracted increasing attention of catalysis community since the multicomposite catalysts generally present greater catalytic proper-

ties in comparison to their single parts due to the synergistic effect among different components.^{28–33} Many studies revealed that the addition of a secondary element to Cu catalysts could significantly improve the selectivity of C₂₊ liquid products for CO₂RR. Ren et al. reported the synergy between Cu and Zn in Cu–Zn bimetallic catalyst significantly promoted the selectivity of ethanol (EtOH) for CO₂RR.²³ Similarly, Morales-Guio et al. claimed that Cu–Au bimetallic catalyst could selectively convert CO₂ into C₂₊ alcohols.²⁴ Despite all these successful studies, several key challenges still remain to overcome.^{22–26} First, the selectivity of C₂₊ liquid products for CO₂RR is far from satisfaction of industry due to the complicated reaction paths of CO₂RR. Second, the detailed

Received: September 18, 2020

Accepted: December 22, 2020

Published: December 30, 2020



mechanism of synergistic effect between different components in composite catalysts for CO₂RR has not been completely understood yet.^{16,34,35} Thus, the design of efficient and robust catalysts based on the synergistic effect for CO₂RR is extremely desirable yet challenging.

In this study, we demonstrated that Cu/Pb core/shell nanocrystals (NCs) could serve as an efficient catalyst for CO₂RR to generate ultrahigh selectivity of C₂₊ liquid products. Experimental results indicated that the synergistic effect between Cu and Pb in a Cu/Pb core/shell NCs significantly improved the selectivity of C₂₊ products. The Faradaic efficiency (FE) of C₂₊ products for CO₂RR reached as high as 73.5% when CuPb-0.7/C was used, much higher than that of pure Cu NCs under the same conditions (42.4%). Moreover, when applying in a flow-cell device with 1 M KOH, the current density and FE of C₂₊ liquid products were 196.8 mA cm⁻² and 49.5%, respectively, outperforming most of the reported Cu-based catalysts for the production of C₂₊ liquid products. Characterizations and DFT calculations revealed that the Cu/Pb core/shell NCs could decrease the formation energy of *COOH and *OCCOH, as two critical intermediates for the formation of C₂₊ products, thus leading to the increase in the selectivity of C₂₊ products.

RESULTS AND DISCUSSION

The Cu/Pb core/shell NCs were prepared *via* the reduction of copper(II) acetylacetone (Cu(acac)₂) and lead dichloride (PbCl₂) in a mixture of ascorbic acid (AA) diphenyl ether (DPE), and oleylamine (OAm) at 190 °C for 3 h. As shown in Figure S1, the time dependent experiment revealed that the Cu NCs were first reduced at the beginning time. Then, the initial Cu NCs was evolved into octahedron and Pb species began to be formed (90 min). At 135 min, the Pb species were further reduced and epitaxially grown on the surface of Cu NCs, forming the Cu/Pb core/shell structure. At 180 min, the NCs further grew and matured into the final Cu/Pb core/shell NCs. By controlling the ratio of Cu/Pb precursors, the thickness of Pb shell can be tuned from 0.7 (CuPb-0.7 NCs) to 1.5 nm (CuPb-1.5 NCs) (Figure 1a), corresponding to about two and four Pb layers deposited on Cu core surface, respectively. Scanning electron microscopy energy-dispersive X-ray spectroscopy (SEM-EDS) measurement indicated that the molar ratios of Cu and Pb in CuPb-0.7 and CuPb-1.5 NCs were 87.6:12.4 and 80.2:19.8, respectively (Figure S2). High-angle annular dark-field scanning transmission electron microscopy (HAADF-STEM) images revealed the octahedral morphologies with high purity (over 90%) of CuPb-0.7 and CuPb-1.5 NCs (Figure 1b). Energy-dispersive X-ray spectroscopy (EDS) mapping measurements confirmed the core/shell structure of CuPb-0.7 and CuPb-1.5 NCs (Figure 1c and S3). High-resolution TEM (HRTEM) images implied that the mean thicknesses of CuPb-0.7 and CuPb-1.5 NCs were ~0.7 and ~1.5 nm, respectively (Figure 1d–g and Figure S4). The lattice distance of 0.209 nm was ascribed to Cu (111) plane, which further confirmed that Cu was core material (Figures 1e and g). The characteristic peaks of Cu and Pb were observed in both the powder X-ray diffraction (XRD) patterns of CuPb-0.7 and CuPb-1.5 NCs (Figure 2a).

Moreover, X-ray photoelectron spectroscopy (XPS) measurement was employed to study the surface properties of CuPb-0.7 and CuPb-1.5 NCs. Two peaks appeared at 951.8 eV in the XPS spectra of CuPb-0.7 and CuPb-1.5 NCs, which could be assigned to Cu⁺/Cu⁰ species (Cu⁺ and Cu⁰ were indistinguishable in XPS spectrum) (Figure 2b).²⁹ Auger electron spectroscopy (AES) measurements were performed to further study the chemical states of Cu on CuPb-0.7 and CuPb-1.5 NCs. An intense peak was observed at ~916.9 eV in the AES spectrum of CuPb-0.7 and at ~917.7 eV in the AES spectrum of CuPb-1.5 NCs (Figure 2c), which suggested that CuPb-0.7 and CuPb-1.5 NCs mainly consisted of Cu⁺ and Cu⁰, respectively.^{15,29} On the other hand, Pb 4f XPS spectra revealed that Pb in the CuPb-0.7 and CuPb-1.5 NCs consisted of Pb²⁺ and Pb⁰ (Figure 2d). Furthermore, the surface redox potentials of the Cu/Pb core/shell NCs were investigated *via* cyclic voltammograms (CVs).

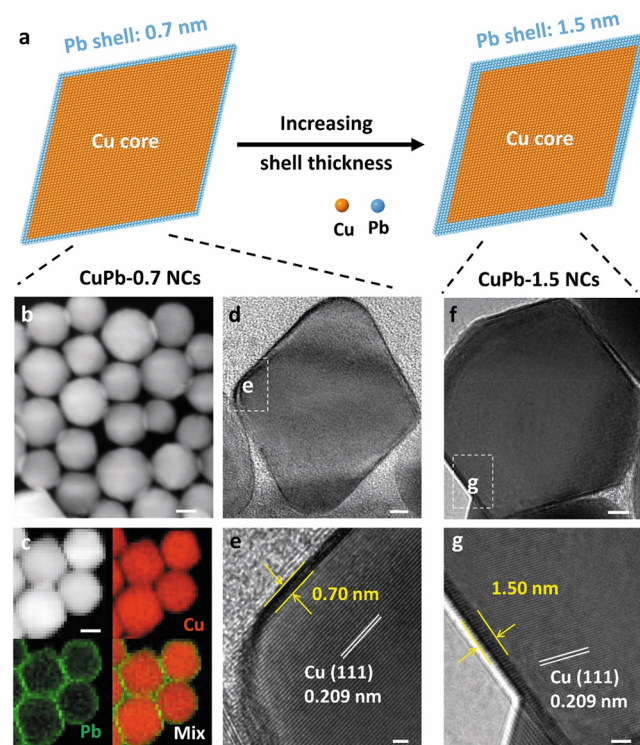


Figure 1. Structure characterizations of Cu/Pb core/shell NCs. (a) Atomic profile model of Cu/Pb core/shell electrocatalysts. (b) HAADF-STEM image, (c) EDS elemental mapping images, (d) HRTEM image, and (e) the magnified HRTEM image in (d) of CuPb-0.7 NCs. (f) HRTEM image and (g) the magnified HRTEM image in (f) of CuPb-1.5 NCs. Scale bars: 1 nm in (f) and (g), 5 nm in (d) and (e), 20 nm in (b) and (c).

and 931.8 eV in the XPS spectra of CuPb-0.7 and CuPb-1.5 NCs, which could be assigned to Cu⁺/Cu⁰ species (Cu⁺ and Cu⁰ were indistinguishable in XPS spectrum) (Figure 2b).²⁹ Auger electron spectroscopy (AES) measurements were performed to further study the chemical states of Cu on CuPb-0.7 and CuPb-1.5 NCs. An intense peak was observed at ~916.9 eV in the AES spectrum of CuPb-0.7 and at ~917.7 eV in the AES spectrum of CuPb-1.5 NCs (Figure 2c), which suggested that CuPb-0.7 and CuPb-1.5 NCs mainly consisted of Cu⁺ and Cu⁰, respectively.^{15,29} On the other hand, Pb 4f XPS spectra revealed that Pb in the CuPb-0.7 and CuPb-1.5 NCs consisted of Pb²⁺ and Pb⁰ (Figure 2d). Furthermore, the surface redox potentials of the Cu/Pb core/shell NCs were investigated *via* cyclic voltammograms (CVs).

Specifically, CuPb-0.7 and CuPb-1.5 NCs were loaded on carbon (VC-X72) (denoted as CuPb-1.5/C and CuPb-0.7/C, respectively) for testing (Figure S5), and Cu/C (Cu NCs loaded on VC-X72) and Pb/C (Pb NCs loaded on VC-X72) were used as references (Figures S6 and S7). Figure 2e exhibits the CVs of different catalysts from -0.2 to +1.0 *versus* a reversible hydrogen electrode (RHE, V_{RHE}) in an Ar-saturated 0.1 M KHCO₃ solution. The anodic and cathodic peaks were observed at 0.82 and 0.55 V_{RHE} in the CV profiles of Cu/C, which corresponded to the oxidation of Cu to CuO and the reduction of CuO to Cu, respectively (Figure 2e).³⁶ Similarly, the anodic and cathodic peaks of Pb/C were observed at 0.24 and 0.14 V_{RHE}, which were ascribed as the oxidation of Pb to PbO and the reduction of PbO to Pb, respectively (Figure 2e).³⁷ Compared with Cu/C catalyst, the Cu redox peaks of

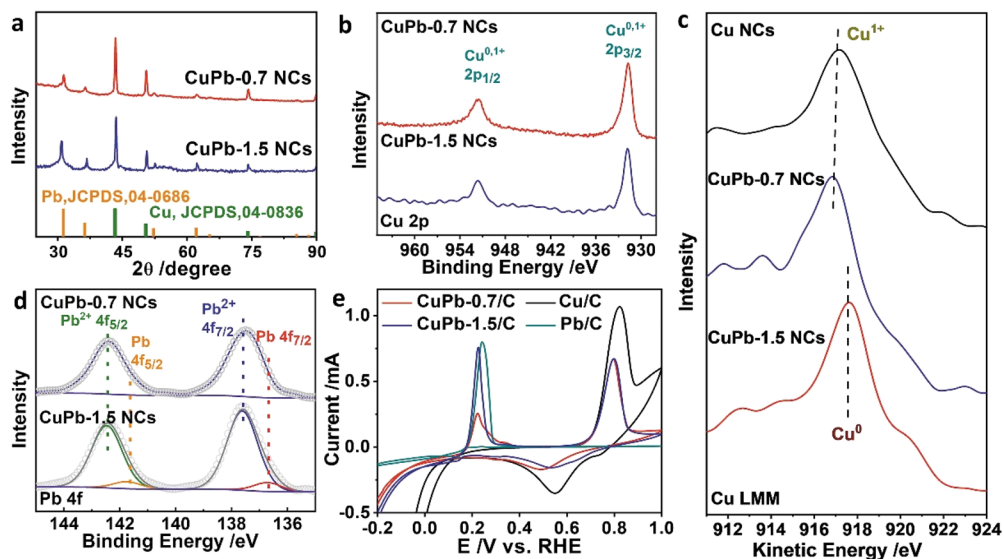


Figure 2. Phase and surface analysis of Cu/Pb core/shell NCs. (a) XRD patterns of CuPb-0.7 and CuPb-1.5 NCs. (b) Cu 2p XPS, (c) Cu LMM AES and (d) Pb 4f XPS curves of CuPb-0.7 and CuPb-1.5 NCs. (e) CV curves of Cu/C, Pb/C, CuPb-0.7/C, and CuPb-1.5/C in Ar-saturated 0.1 M KHCO₃ solution. Scan rate is 50 mV/s.

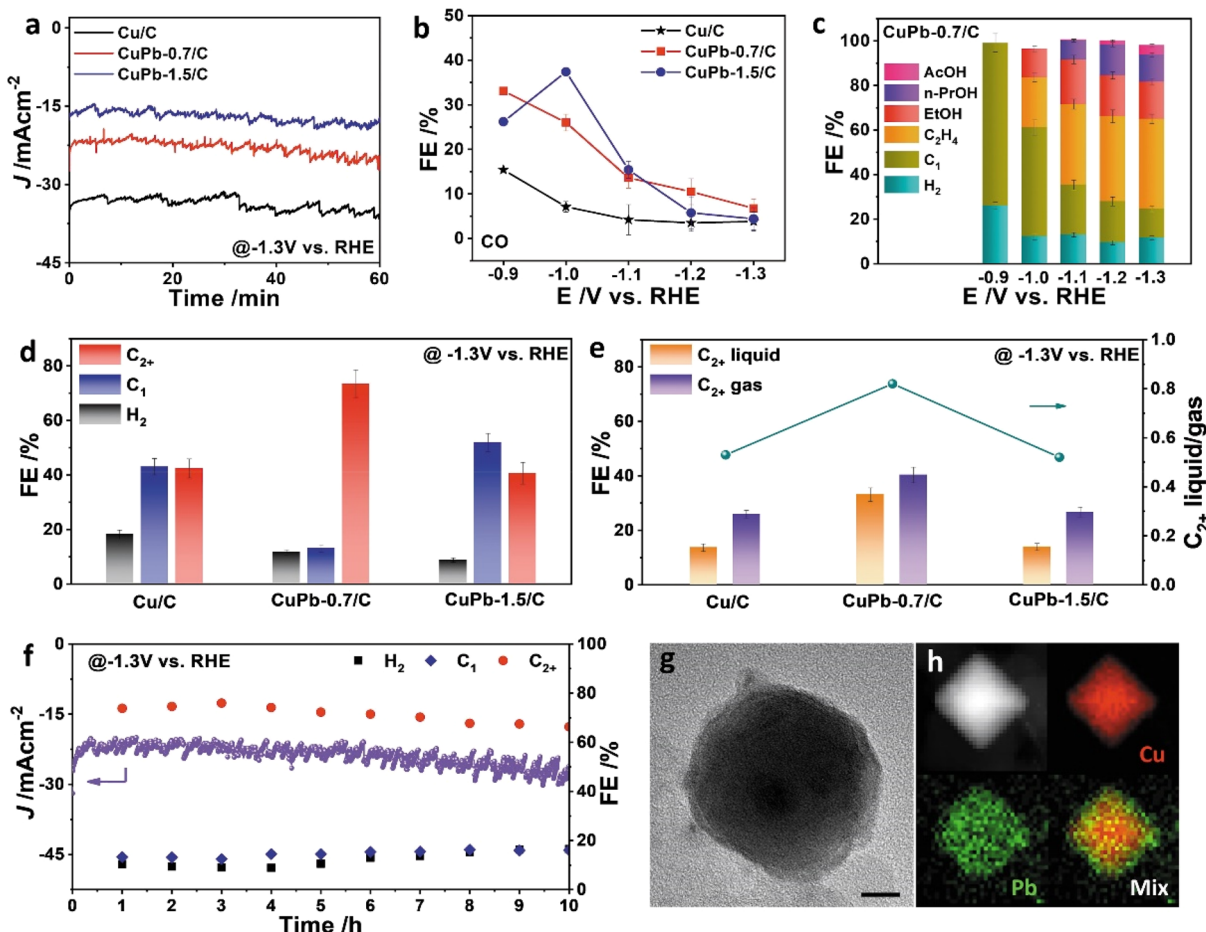


Figure 3. CO₂RR performance of CuPb-0.7/C. (a) Chronoamperometry curves of Cu/C, CuPb-0.7/C, and CuPb-1.5/C. (b) FEs of CO at different applied potentials for Cu NPs/C, CuPb-0.7/C, and CuPb-1.5/C. (c) FEs of products for CO₂RR under different applied potentials over CuPb-0.7/C. (d) FEs of H₂, C₁, and C₂₊ and (e) C₂₊ liquid and C₂₊ gaseous products for Cu/C, CuPb-0.7/C and CuPb-1.5/C at -1.3 V_{RHE}. (f) Stability test of CuPb-0.7/C for CO₂RR at -1.3 V_{RHE}. (g) TEM image and (h) element mapping image of CuPb-0.7/C after stability test. Scale bar was 10 nm in (g). The chronoamperometry curves were recorded with 50% insulation resistance compensation and the current densities were normalized to the geometric area of working electrode (0.196 cm²).

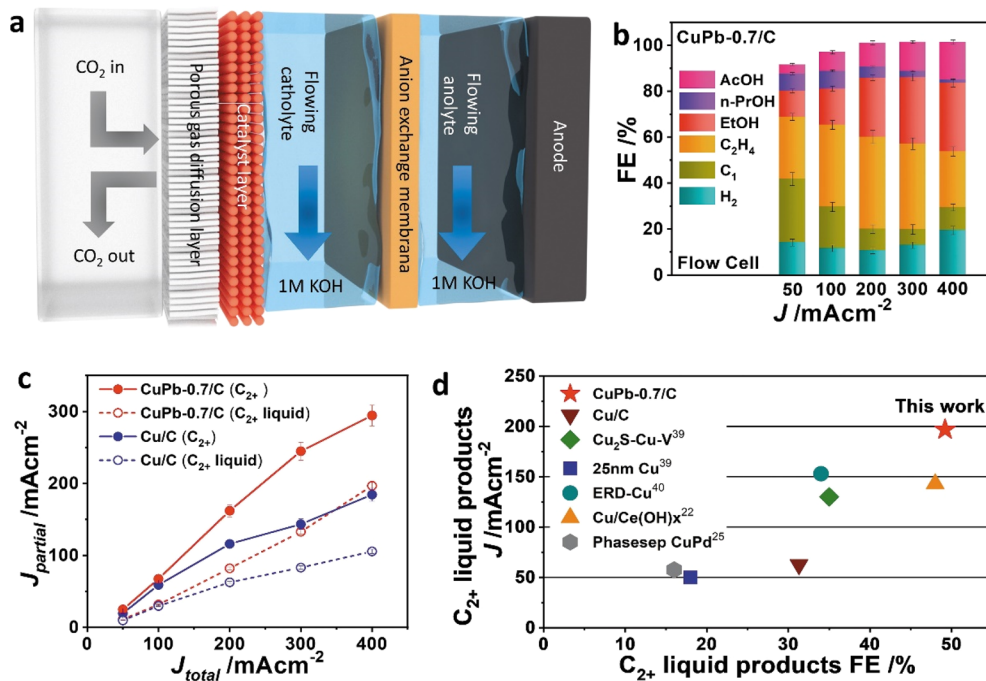


Figure 4. CO_2RR_2 performance in a flow-cell system over CuPb-0.7/C. (a) Schematic illustration of the cathode flow-cell system using a gas-diffusion electrode. (b) FEs of products for CO_2RR in the current density range of 50–400 mA cm^{-2} over CuPb-0.7/C. (c) Partial current densities of total C_{2+} products and C_{2+} liquid products for CO_2RR in the current density range of 50–400 mA cm^{-2} over CuPb-0.7/C and Cu/C. (d) Plot of the partial current density of C_{2+} liquid products *versus* the maximum FE of C_{2+} liquid products for different electrocatalysts in a flow cell system with 1 M KOH.

CuPb-0.7/C and CuPb-1.5/C still existed but significantly weakened, suggesting part of the Cu atoms were still exposed on the surface though most of them were covered by the Pb shell. In addition, the oxidation peaks (Pb to PbO) of CuPb-0.7/C and CuPb-1.5/C were more negative than that of Pb/C, which indicated that electrons transfer between the Cu core and Pb shell might occur.

Afterward, CO_2RR over the CuPb-0.7/C and CuPb-1.5/C were tested in a H-cell system. The electrocatalysts were loaded on an L-type glassy-carbon electrode and subsequently tested in 0.1 M KHCO_3 *via* the chronoamperometry method under different potentials (Figure S8). The gaseous and liquid products were analyzed by gas chromatography (GC) and nuclear magnetic resonance (NMR) measurements, respectively (Figures S9 and S10). As depicted in Figure 3a, the geometric current densities (the current normalized to the geometric area of working electrode) of CuPb-1.5/C, CuPb-0.7/C, and Cu/C displayed an order of Cu/C > CuPb-0.7/C > CuPb-1.5/C, indicating that the coating Cu with Pb shell affected the CO_2RR activity. Nevertheless, the FEs of CO for CuPb-0.7/C and CuPb-1.5/C were obviously increased compared to the Cu/C under the same conditions, suggesting that the coating of Pb shell could effectively promote the formation of *CO intermediates, which is the necessary reaction intermediate for C_{2+} products generation *via* the further C–C coupling process (Figure 3b). Consequently, the FE of total C_{2+} products for CuPb-0.7/C reached 73.5% at $-1.3 \text{ V}_{\text{RHE}}$, in which C_2H_4 , EtOH, *n*-propanol (*n*-PrOH), and acetic acid (AcOH) accounted for 40.3%, 16.7%, 12.1% and 4.4%, respectively (Figure 3c). To the best of our knowledge, the current CuPb-0.7/C outperformed Cu/C and most of the reported Cu-based catalysts for CO_2RR to produce C_{2+} products (Figure S11 and S12). In addition, the FEs of H_2 ,

C_1 and C_{2+} products for Cu/C, CuPb-0.7/C and CuPb-1.5/C were further compared in Figure 3d. Compared to Cu/C catalyst, the decrease in the H_2 FEs for CuPb-0.7/C and CuPb-1.5/C suggested that the Pb shell significantly suppressed hydrogen evolution reaction (HER). However, once the Pb shell was increased to 1.1 or 1.5 nm, the FE of C_{2+} products gradually decreased and more formate was generated (Figure S13 and Figure S14), approaching to the CO_2RR performance of Pb/C (Figure S15). Therefore, with increasing the Pb shell thickness, the FEs of C_{2+} products show a volcanic curve, while the FEs of HCOOH present the opposite trend (Figure S16). Hence, the optimal thickness of Pb shell in Cu/Pb core/shell is important to achieve the C_{2+} products. Moreover, the ratio of liquid and gaseous C_{2+} products for CO_2RR at $-1.3 \text{ V}_{\text{RHE}}$ over CuPb-0.7/C was 0.82, which was much higher than those of Cu/C (0.53) and CuPb-1.5/C (0.52) (Figure 3e). These aforementioned results indicated that CuPb-0.7/C could be used as a highly selective catalyst for CO_2RR to produce liquid C_{2+} products. Furthermore, the stability of CuPb-0.7/C for CO_2RR at $-1.3 \text{ V}_{\text{RHE}}$ was tested, and no significant decays in the FEs of C_{2+} products (C_2H_4 , EtOH, *n*-PrOH, and AcOH) or the morphology of the spent catalyst were observed after 10 h continuous electrocatalysis (Figures 3f, S17, and S18), which suggested the excellent stability of CuPb-0.7/C.

CO_2RR over CuPb-0.7/C was further tested in a flow-cell system to study the potential application in industry (Figure 4a).³⁸ We first deposited the catalysts by spray-coating a configure ink onto a carbon gas diffusion electrode (GDE), and the details are given in the Supporting Information. Afterward, CO_2RR performance was evaluated in the current density range (50–400 mA cm^{-2}) in 1 M KOH *via* a chronopotentiometry test (Figure S19). The total FE of C_{2+} liquid product was 49.5% at a current density of 400 mA cm^{-2}

when CuPb-0.7/C was used, in which EtOH, n-PrOH, and AcOH accounted for 29.9%, 1.43%, and 16.3%, respectively (Figure 4b). In contrast, the total FE of C_{2+} liquid product was 26.4% under the aforementioned conditions (Figure S20). Moreover, the partial current densities of CuPb-0.7/C for total C_{2+} and C_{2+} liquid products were 294.4 and 196.8 mA cm⁻², respectively, which were 1.60-fold and 1.86-fold higher than those of Cu/C under same conditions (Figure 4c). The plots of partial current density for C_{2+} liquid products *versus* the maximum FE for C_{2+} liquid products suggested that the current CuPb-0.7/C catalyst was more selective than the reported catalysts for the production of C_{2+} liquid products (Figure 4d).^{22,25,39,40}

The operando X-ray absorption (XAS) spectroscopy measurement was performed to study the structure evolution of CuPb-0.7/C during electrocatalysis. Cu species in CuPb-0.7/C were reduced into metallic Cu after 15 min of CO₂RR at -1.3 V_{RHE} (Figure S21). Moreover, the metallic state Cu cannot be oxidized when the applied potential was removed (Figure S21). In addition, CO₂ and CO temperature-programmed desorption (CO₂-TPD and CO-TPD) for CuPb-0.7/C and CuPb-1.5/C were carried out to investigate the adsorption capacity of CO₂ and CO on catalysts. As shown in Figure S22, both CuPb-0.7/C and CuPb-1.5/C display the desorption peaks at around 288 and 286 °C. However, for the CuPb-0.7/C, it appears other desorption peaks at high temperatures (310 and 312 °C) for CO₂-TPD and CO-TPD, respectively. According to the reported studies and existed results,^{41,42} the former peaks can be attributed to the chemical adsorption of CO₂ and CO on Pb shell, respectively, while the high temperature peaks are attributed to the chemical adsorption of CO₂ and CO on Cu/Pb interfaces. This result suggests that the CuPb-0.7/C has strong bonding strength to CO₂ and CO, which is propitious to further reduce them into C_{2+} products during CO₂RR. Finally, the contrast experiments were performed to transform the Cu/Pb core/shell nanostructure into the Cu/Pb heterostructure (CuPb-0.7/C-AH) *via* a thermal treatment (Figure S23), in order to identify the effect of Cu/Pb core/shell structure for the selectivity improvement. As a result, when CuPb-0.7/C-AH was used as catalyst, the selectivity of CO and C_{2+} products was obviously decreased (Figure S24), indicating that the core/shell structure involved synergistic effect between Cu and Pb is crucial to the selectivity enhancement. On the basis of the collective analyses, an assumptive process for C_{2+} species generation on CuPb-0.7/C can be proposed. The optimal interfaces between Cu and Pb on the core/shell CuPb-0.7/C could serve as the catalytic site to adsorb, activate and convert CO₂ into CO or its intermediates. Once the *in situ* formed CO or intermediates accumulate around the interface, the C–C coupling would be further promoted by the Cu/Pb synergistic effect, thus improving the CO₂RR activity and selectivity for C_{2+} products.

DFT calculations were performed to further identify our supposition and study the potential mechanism for CO₂RR. The solvation effect was taken into consideration in DFT calculations using an implicit water molecule model (see more details in the Supporting Information). First, we constructed the theoretical models for CuPb-0.7/C and pure Cu NCs. A 4 × 3 × 4 (111) surface slab model was selected for the pure Cu system. For the CuPb-0.7/C model, the bottom layer and upper layer consisted of 4 × 3 × 2 Cu (111) and 3 × 2 × 2 Pb (111) slab models, respectively. Moreover, one Pb atom was replaced by Cu in each Pb layer to mimic the core/shell

structure of CuPb-0.7/C. Second, we calculated the formation energy of *COOH, a critical intermediate for the formation of CO,⁴³ for pure Cu and Cu/Pb systems to study the activity. The formation energy of *COOH for Cu/Pb system was 0.18 eV lower than that of pure Cu system, which suggested that the synergy between Cu and Pb could promote the CO₂RR activity (Figure 5a). Furthermore, the formation energy of

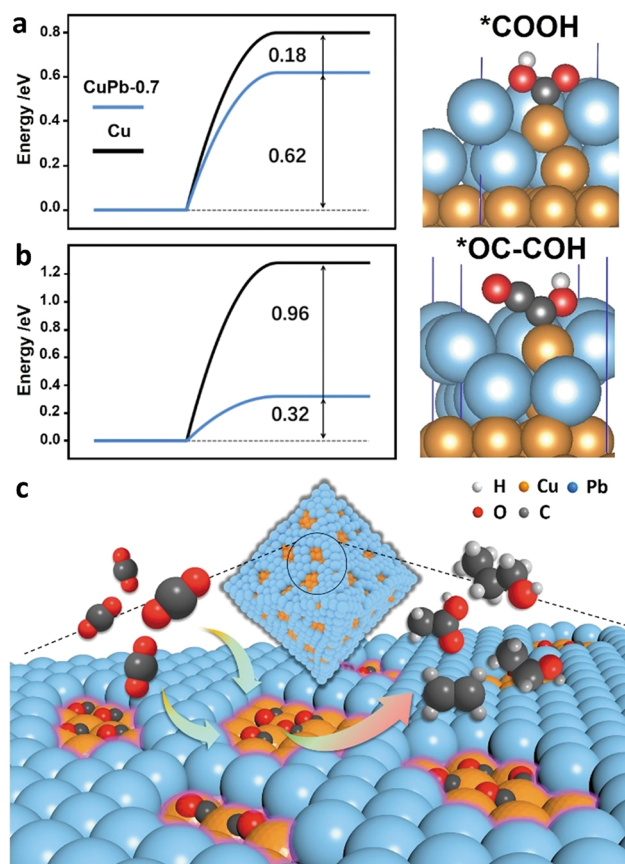


Figure 5. Theoretical simulations and schematic illustration for the CO₂RR. (a) Free energy of *COOH formation (left) and the optimized adsorption structure (right) for CuPb-0.7/C and Cu/C catalysts. (b) Free energy of *OC-COH formation (left) and the optimized adsorption structure of *OC-COH (right) for CuPb-0.7/C and Cu/C. (c) Schematic illustration of CO₂RR over Cu/Pb core/shell NCs.

*OCCOH, a critical intermediate for the formation of C_{2+} products was calculated.⁴⁴ The formation energy of *OCCOH for Cu/Pb system was 0.32 eV, which was significantly lower than that of pure Cu system (0.96 eV) (Figure 5b). In addition, the intact reaction pathways for CO₂ reduction on Cu and CuPb-0.7 also show that the formation energies of the key intermediates with respect to CO, ethylene and ethanol on the Cu/Pb surface are almost lower than those on pure Cu surface (Figure S24). These aforementioned results suggested that the synergy between Cu and Pb on CuPb-0.7/C significantly promoted the reduction of CO₂ into CO through the intermediate of *COOH, which was further converted into C_{2+} products *via* the formation of *OCCOH (Figure 5c).

CONCLUSION

In summary, we demonstrated that the synergistic effect between Cu and Pb on Cu/Pb core/shell NCs, which

significantly boosted CO₂RR to produce C₂₊ products, especially liquid C₂₊ products. The total FE of C₂₊ products and partial current density were 73.5% and 294.4 mA cm⁻², respectively, for CO₂RR in a flow cell system over CuPb-0.7/C. Moreover, the FE and partial current density of C₂₊ liquid products reached 49.5% and 196.8 mA cm⁻², respectively, and outperforming most of the reported Cu-based catalysts for CO₂RR toward the production of C₂₊ liquid products. The operando XAS measurements and DFT calculations suggested that the synergy between Cu and Pb on CuPb-0.7/C significantly promoted the reduction of CO₂ into CO through the intermediate of *COOH, which was further converted into C₂₊ products *via* the formation of *OCCOH. This study provides an efficient Cu-based catalyst for the reduction of CO₂ and also highlights the importance of synergistic effect for the design of electrocatalysts in catalysis.

MATERIALS AND METHODS

Materials. Copper(II) acetylacetone (Cu(acac)₂, 97%), ascorbic acid (AA, AR), diphenyl ether (DPE, 98%), and oleylamine (CH₃(CH₂)₁₁CH = CH(CH₂)₁₁CH₂NH₂, 70%) were purchased from Sigma-Aldrich. Potassium bicarbonate (KHCO₃, AR) and potassium hydroxide (KOH, AR) were purchased from Sinopharm Chemical Reagent Co. Ltd. (Shanghai, China). Lead dichloride (PbCl₂) and lead acetate (Pb(ac)₂·3H₂O) were purchased from Strem Chemical. N₂ (99.999%) and CO₂ (99.999%) were provided by WuGang Gas Co., Ltd. (Shanghai, China). All of the chemicals were used as received without further purification. Ultrapure water (18 MΩ·cm) was used in all experiments.

Preparation of CuPb NCs. In a typical preparation of CuPb-0.7 NCs, 13.3 mg of Cu(acac)₂, 4 mg of PbCl₂, 27 mg of AA, 1 mL of diphenyl ether, and 4 mL of oleylamine were added into a 30 mL vial. After the vial had been capped, the mixture was ultrasonicated for around 0.5 h. The resulting homogeneous mixture was then heated at 190 °C for 3 h in an oil bath before it was cooled to room temperature. The resulting colloidal products were collected by centrifugation and washed with ethanol/cyclohexane mixture. The preparation of CuPb-1.5 and CuPb-1.1 NCs was similar to that of CuPb-0.7 NCs except for adding 7 and 5.5 mg of PbCl₂, respectively.

Preparation of CuPb-0.7/C, CuPb-1.5/C, and CuPb-0.7/C-AH. In a typical preparation of CuPb-0.7/C, CuPb-0.7 NCs and VC-X72 carbon were mixed in 10 mL of cyclohexane and sonicated for 1 h to deposit NPs on carbon. The products were separated by centrifugation and washed with cyclohexane/ethanol to generate CuPb-0.7/C. The preparation of CuPb-1.5/C is similar to that of CuPb-0.7/C by mixing the CuPb-1.5 NCs with VC-X72 carbon. The CuPb-0.7/C was subjected to a thermal annealing in air at 250 °C for 1 h and a subsequent thermal annealing in 5% H₂ + 95% N₂ at 350 °C for another 1 h to obtain CuPb-0.7/C-AH. The mass loadings (65.8% ± 0.5%) in all the catalysts were determined by ICP-AES inductively coupled plasma-atomic emission spectrometry measurement.

Preparation of Cu NCs and Cu/C. The preparation method for Cu NCs was similar to that of CuPb NCs except for the absence of PbCl₂. The resulting products were collected by centrifugation and washed with ethanol/cyclohexane mixture. For Cu/C, the obtained Cu NCs and VC-X72 carbon were then mixed in 10 mL of cyclohexane and sonicated for 1 h to deposit Cu NCs on carbon. The products were separated by centrifugation and washed with cyclohexane/ethanol to generate Cu/C.

Preparation of Pb NCs and Pb/C. In a typical preparation of Pb NCs, 19 mg of Pb(ac)₂, 73 mg of AA, and 5 mL of oleylamine were added into a 30 mL vial. After the vial had been capped, the mixture was ultrasonicated for around 0.5 h. The resulting homogeneous mixture was then heated at 190 °C for 3 h in an oil bath before it was cooled to room temperature. The resulting colloidal products were collected by centrifugation and washed with ethanol/cyclohexane mixture. For the preparation of Pb/C, the Pb NCs, 36.5 mg of AA (prevent the oxidation of Pb) and VC-X72 carbon were then mixed in

10 mL of cyclohexane and sonicated for 1 h to deposit Pb NCs on carbon. The products were separated by centrifugation and washed with cyclohexane/ethanol.

Characterizations. TEM and HAADF-STEM were conducted on a FEI Tecnai F20 transmission electron microscope with acceleration voltage of 200 kV. The samples were prepared by dropping cyclohexane or ethanol dispersion of samples onto carbon-coated copper TEM grids using pipettes and dried under ambient condition. XRD patterns were collected on X'Pert-Pro MPD diffractometer (Netherlands PANalytical) with a Cu K α X-ray source (λ = 1.540598 Å). The concentrations of catalysts were determined by the inductively coupled plasma atomic emission spectroscopy (710-ES, Varian, ICP-AES). XPS was done with an SSI S-Probe XPS Spectrometer. The carbon peak at 284.6 eV was used as a reference to correct for charging effects. XAS data were collected at the TPS-44A beamline of the National Synchrotron Radiation Research Center (NSRRC, Hsinchu, Taiwan) using a Si (111) quick-scanning monochromator. Data were processed according to standard procedures using the Demeter program package (Version 0.9.24).

CO₂ Electrocatalysis in H-Cell. A three-electrode system was used to perform the electrochemical CO₂ reduction in H cell. A L-type glassy-carbon electrode (5 mm, 0.196 cm²) was used as working electrode. A micro Ag/AgCl electrode (4.0 M KCl) and a Pt wire were used as reference electrode and counter electrode, respectively. The catalyst ink was prepared by ultrasonication 2 mg of catalyst with 490 μL of ethanol and 10 μL of 5 wt % Nafion solutions for 1 h. A 50 μL suspension was then deposited on carbon paper to prepare the working electrodes. Electrochemical reduction of CO₂ was conducted in a gastight H-cell separated by a cation exchange membrane (Nafion 117) on a CHI660 (Chenhua, Shanghai) electrochemical workstation. Each chamber contained 20 mL of 0.1 M KHCO₃ aqueous solution with a ~30 mL headspace. As for the electrochemical measurements, the CO₂ was delivered into the cathodic compartment (directly connected to gas chromatograph (GC Agilent 7890B)) at a constant rate of 20 sccm and was allowed to purge for 30 min prior to the beginning of experiments. Then, the reactions were tested by the chronoamperometry method under different potentials. The gas phase composition was analyzed by GC equipped with a PLOT MolSieve 5A column and a Q-bond PLOT column every 15 min with different potential applied. Liquid products were characterized by ¹H NMR on Agilent 600 MHz DirectDrive2 spectrometers. ¹H chemical shifts were referenced to residual protic solvent signals. All potentials were given against the reversible hydrogen electrode (RHE), calculated using the Nernst equation and the readouts were recorded with 50% ohmic *iR* drop correction. The faradaic efficiency (FE) for the formation of a hydrocarbon was calculated as follows: FE = *eF* × *n*/*Q* = *eF* × *n*/(*I* × *t*), where *e* is the number of electrons transferred, *F* is the Faraday constant, *Q* is the charge, *I* is the current, *t* is the running time, and *n* is the total amount of product (in moles).

CO₂ Electrocatalysis in Flow Cell. Electrocatalysis was performed in a flow cell configuration that consisted of a catalyst-deposited GDE as the working electrode, an anion-exchange membrane (Fumasep FAB-PK-130), and nickel foam (1 mm thickness) as the anode. GDEs were prepared by loading catalysts onto a gas diffusion layer (CeTech, NIS1007) *via* an airbrush technique. Catalysts' ink was prepared by mixing 3 mg of catalyst, 10 μL of 5 wt % Nafion solutions, and 1 mL of ethanol. The ink was sonicated for 30 min before airbrushing. Well-dispersed ink was then airbrushed onto a piece of gas diffusion layer (2 × 2.5 cm²) using an airbrush pumped by nitrogen at a fixed pressure of 20 p.s.i. The loading amount was determined by weighing the gas diffusion layer before and after airbrushing (mass loading: 0.37 mg_{Cu} cm⁻² for CuPb-0.7/C and 0.35 mg_{Cu} cm⁻² for Cu/C). The GDE with catalysts, anion exchange membrane and nickel anode were then positioned and clamped together using polytetrafluoroethylene spacers. Thus, a liquid electrolyte could be introduced into the chambers between the anode and membrane as well as between the membrane and cathode. Gaseous CO₂ was then passed behind the gas diffusion layer to diffuse into the liquid electrolyte presented at the catalytic area (0.5 × 2 cm²). In the catholyte stream, a port drilled into the polytetrafluoro-

ethylene spacer allowed a micro reference Ag/AgCl electrode (4.0 M KCl) to be positioned at a specific distance from the working electrode. All the electrochemical experiments were performed using a CHI660 (Chenhua, Shanghai) electrochemical workstation with a current amplifier. The electrolyte (1 M KOH solution, 20 mL for each of the catholyte and anolyte) was circulated through the electrochemical cell using peristaltic pumps. The electrolyte flow was kept at 25 mL min⁻¹. CO₂ flow was kept constant at 30 mL min⁻¹ with a mass flow controller. The reactions were tested by chronopotentiometry method at different currents for 1 h without ohmic iR drop correction. The methods for analyzing liquid and gaseous products in flow cell were the same as those in H cell.

Computational Method. The *ab initio* quantum mechanical calculations were performed by using Vienna *ab Initio* Simulation Package (VASP)^{45–48} at a version of 5.4.4 with the projector augmented wave method and a plane wave basis set. The method was density functional theory (DFT) with generalized gradient approximations of Perdew–Burke–Ernzerhof functional.^{49,50} A dispersion correction, DFT-D3 method with Becke–Jonson damping⁵¹ was included in the calculations. The energy cutoff was set to 400 eV. Spin polarization did not have an appreciable effect on the overall energies and thus was not included in the calculations. The electronic self-consistent step was considered to be converged when both the changes of total energy and eigenvalues between two steps were smaller than 1 e⁻⁵ eV. The partial occupancies for each orbital were set with first-order Methfessel–Paxton scheme in the smearing width of the 0.2 eV. The dipole moment corrections for the total energy are considered in the direction normal to the surface. A conjugate-gradient algorithm was used to relax the ions in energy minimization. The minimization was considered to be converged when all the forces were smaller than 1 e⁻⁴ eV/Å. The implicit solvation model of VASPsol was employed to describe the effect of electrostatics, cavitation, and dispersion on the interaction between a solute and solvent.^{52,53} The relative permittivity of the solvent and the Debye screening length were 78.4 and 3.0 Å, respectively. The number of electrons in the simulations were tuned to match the target chemical potential of electron.

ASSOCIATED CONTENT

Supporting Information

The Supporting Information is available free of charge at <https://pubs.acs.org/doi/10.1021/acsnano.0c07869>.

Detailed information on diameter statistics, shell thickness analysis, composition analysis, morphology and phase characterizations, CO₂RR products analysis, and CO₂RR performance for Cu/Pb core/shell catalysts and compared catalysts ([PDF](#))

AUTHOR INFORMATION

Corresponding Authors

Xiaoqing Huang – College of Chemistry, Chemical Engineering and Materials Science, Soochow University, Jiangsu 215123, P.R. China; College of Chemistry and Chemical Engineering, Xiamen University, Xiamen 361005, P.R. China; [orcid.org/0000-0003-3219-4316](#); Email: hxq006@xmu.edu.cn

Qi Shao – College of Chemistry, Chemical Engineering and Materials Science, Soochow University, Jiangsu 215123, P.R. China; Guangdong Provincial Key Laboratory of Energy Materials for Electric Power, Southern University of Science and Technology, Shenzhen 518055, P.R. China; [orcid.org/0000-0002-9858-0458](#); Email: qshao@suda.edu.cn

Authors

Pengtang Wang – College of Chemistry, Chemical Engineering and Materials Science, Soochow University, Jiangsu 215123, P.R. China; College of Chemistry and Chemical Engineering, Xiamen University, Xiamen 361005, P.R. China

Hao Yang – Institute of Functional Nano & Soft Materials (FUNSOM), Soochow University, Jiangsu 215123, P.R. China; [orcid.org/0000-0002-8241-6231](#)

Yong Xu – Guangzhou Key Laboratory of Low-Dimensional Materials and Energy Storage Devices, Collaborative Innovation Center of Advanced Energy Materials, School of Materials and Energy, Guangdong University of Technology, Guangzhou 510006, Guangdong, P.R. China; [orcid.org/0000-0001-5115-6492](#)

Juan Wang – College of Chemistry, Chemical Engineering and Materials Science, Soochow University, Jiangsu 215123, P.R. China

Miao Zhong – College of Engineering and Applied Sciences, Nanjing University, Jiangsu 215093, P.R. China

Tao Cheng – Institute of Functional Nano & Soft Materials (FUNSOM), Soochow University, Jiangsu 215123, P.R. China; [orcid.org/0000-0003-4830-177X](#)

Complete contact information is available at:
<https://pubs.acs.org/10.1021/acsnano.0c07869>

Author Contributions

[#]P.W., H.Y., and Y.X. contributed equally to this work.

Notes

The authors declare no competing financial interest.

ACKNOWLEDGMENTS

This work was financially supported by the Ministry of Science and Technology (2017YFA0208200, 2016YFA0204100), the National Natural Science Foundation of China (21571135, 21905188, 21975148), Natural Science Foundation of Jiangsu Higher Education Institutions (SBK20190810), Young Thousand Talented Program, Jiangsu Province Natural Science Fund for Distinguished Young Scholars (BK20170003), Jiangsu Province High-Level Talents (JNHB-106), China Postdoctoral Science Foundation Grant (2019M651937, 2019M660128), Guangdong Provincial Key Laboratory of Energy Materials for Electric Power (No. 2018B030322001), the Priority Academic Program Development of Jiangsu Higher Education Institutions (PAPD), the Program for Jiangsu Specially-Appointed Professors to T.C., start-up support from Soochow University and Collaborative Innovation Center of Suzhou Nano Science and Technology.

REFERENCES

- (1) Arakawa, H.; Aresta, M.; Armor, J. N.; Bartea, M. A.; Beckman, E. J.; Bell, A. T.; Bercaw, J. E.; Creutz, C.; Dinjus, E.; Dixon, D. A.; Domen, K.; DuBois, D. L.; Eckert, J.; Fujita, E.; Gibson, D. H.; Goddard, W. A.; Goodman, D. W.; Keller, J.; Kubas, G. J.; Kung, H. H.; et al. Catalysis Research of Relevance to Carbon Management: Progress, Challenges, and Opportunities. *Chem. Rev.* **2001**, *101*, 953–996.
- (2) Jouny, M.; Luc, W.; Jiao, F. General Techno-Economic Analysis of CO₂ Electrolysis Systems. *Ind. Eng. Chem. Res.* **2018**, *57*, 2165–2177.
- (3) Qiao, J.; Liu, Y.; Hong, F.; Zhang, J. A Review of Catalysts for the Electroreduction of Carbon Dioxide to Produce Low-Carbon Fuels. *Chem. Soc. Rev.* **2014**, *43*, 631–675.

- (4) Stolarczyk, J. K.; Bhattacharyya, S.; Polavarapu, L.; Feldmann, J. Challenges and Prospects in Solar Water Splitting and CO₂ Reduction with Inorganic and Hybrid Nanostructures. *ACS Catal.* **2018**, *8*, 3602–3635.
- (5) Hori, Y.; Vayenas, C.; White, R.; Gamboa-Aldeco, M. Electrochemical CO₂ Reduction on Metal Electrodes. *Mod. Aspects Electroc.* **2008**, *42*, 89–189.
- (6) Sun, Z.; Ma, T.; Tao, H.; Fan, Q.; Han, B. Fundamentals and Challenges of Electrochemical CO₂ Reduction Using Two-Dimensional Materials. *Chem.* **2017**, *3*, 560–587.
- (7) Kuhl, K. P.; Hatsukade, T.; Cave, E. R.; Abram, D. N.; Kibsgaard, J.; Jaramillo, T. F. Electrocatalytic Conversion of Carbon Dioxide to Methane and Methanol on Transition Metal Surfaces. *J. Am. Chem. Soc.* **2014**, *136*, 14107–14113.
- (8) Zhu, Q.; Ma, J.; Kang, X.; Sun, X.; Liu, H.; Hu, J.; Liu, Z.; Han, B. Efficient Reduction of CO₂ into Formic Acid on a Lead or Tin Electrode Using an Ionic Liquid Catholyte Mixture. *Angew. Chem., Int. Ed.* **2016**, *55*, 9012–9016.
- (9) Verma, S.; Hamasaki, Y.; Kim, C.; Huang, W.; Lu, S.; Jhong, H.-R. M.; Gewirth, A. A.; Fujigaya, T.; Nakashima, N.; Kenis, P. J. Insights into the Low Overpotential Electroreduction of CO₂ to CO on a Supported Gold Catalyst in an Alkaline Flow Electrolyzer. *ACS Energy Lett.* **2018**, *3*, 193–198.
- (10) Geng, Z.; Kong, X.; Chen, W.; Su, H.; Liu, Y.; Cai, F.; Wang, G.; Zeng, J. Oxygen Vacancies in ZnO Nanosheets Enhance CO₂ Electrochemical Reduction to CO. *Angew. Chem., Int. Ed.* **2018**, *57*, 6054–6059.
- (11) Nitopi, S.; Bertheussen, E.; Scott, S. B.; Liu, X.; Engstfeld, A. K.; Horch, S.; Seger, B.; Stephens, I. E.; Chan, K.; Hahn, C.; Nørskov, J. K.; Jaramillo, T. F.; Chorkendorff, I. Progress and Perspectives of Electrochemical CO₂ Reduction on Copper in Aqueous Electrolyte. *Chem. Rev.* **2019**, *119*, 7610–7672.
- (12) Kuhl, K. P.; Cave, E. R.; Abram, D. N.; Jaramillo, T. F. New Insights into the Electrochemical Reduction of Carbon Dioxide on Metallic Copper Surfaces. *Energy Environ. Sci.* **2012**, *5*, 7050–7059.
- (13) Dinh, C.-T.; Burdyny, T.; Kibria, M. G.; Seifitokaldani, A.; Gabardo, C. M.; De Arquer, F. P. G.; Kiani, A.; Edwards, J. P.; De Luna, P.; Bushuyev, O. S.; Zou, C.; Quintero-Bermudez, R.; Pang, Y.; Sinton, D.; Sargent, E. H. CO₂ Electroreduction to Ethylene via Hydroxide-Mediated Copper Catalysis at an Abrupt Interface. *Science* **2018**, *360*, 783–787.
- (14) Ma, W.; Xie, S.; Liu, T.; Fan, Q.; Ye, J.; Sun, F.; Jiang, Z.; Zhang, Q.; Cheng, J.; Wang, Y. Electrocatalytic Reduction of CO₂ to Ethylene and Ethanol through Hydrogen-Assisted C-C Coupling over Fluorine-Modified Copper. *Nat. Catal.* **2020**, *3*, 478–487.
- (15) Jung, H.; Lee, S. Y.; Lee, C. W.; Cho, M. K.; Won, D. H.; Kim, C.; Oh, H.-S.; Min, B. K.; Hwang, Y. J. Electrochemical Fragmentation of Cu₂O Nanoparticles Enhancing Selective C-C Coupling from CO₂ Reduction Reaction. *J. Am. Chem. Soc.* **2019**, *141*, 4624–4633.
- (16) Gao, D.; Arán-Ais, R. M.; Jeon, H. S.; Cuenya, B. R. Rational Catalyst and Electrolyte Design for CO₂ Electroreduction towards Multicarbon Products. *Nat. Catal.* **2019**, *2*, 198–210.
- (17) Bushuyev, O. S.; De Luna, P.; Dinh, C. T.; Tao, L.; Saur, G.; van de Lagemaat, J.; Kelley, S. O.; Sargent, E. H. What Should We Make with CO₂ and How Can We Make It? *Joule* **2018**, *2*, 825–832.
- (18) Schouten, K. J. P.; Calle-Vallejo, F.; Koper, M. A. Step Closer to the Electrochemical Production of Liquid Fuels. *Angew. Chem., Int. Ed.* **2014**, *53*, 10858–10860.
- (19) Birdja, Y. Y.; Pérez-Gallent, E.; Figueiredo, M. C.; Göttle, A. J.; Calle-Vallejo, F.; Koper, M. T. Advances and Challenges in Understanding the Electrocatalytic Conversion of Carbon Dioxide to Fuels. *Nat. Energy* **2019**, *4*, 732–745.
- (20) Vasileff, A.; Xu, C.; Jiao, Y.; Zheng, Y.; Qiao, S. Z. Surface and Interface Engineering in Copper-Based Bimetallic Materials for Selective CO₂ Electroreduction. *Chem.* **2018**, *4*, 1809–1831.
- (21) Duan, Y. X.; Meng, F. L.; Liu, K. H.; Yi, S. S.; Li, S. J.; Yan, J. M.; Jiang, Q. Amorphizing of Cu Nanoparticles toward Highly Efficient and Robust Electrocatalyst for CO₂ Reduction to Liquid Fuels with High Faradaic Efficiencies. *Adv. Mater.* **2018**, *30*, 1706194.
- (22) Luo, M.; Wang, Z.; Li, Y. C.; Li, J.; Li, F.; Lum, Y.; Nam, D.-H.; Chen, B.; Wicks, J.; Xu, A.; Zhuang, T.; Leow, W. R.; Wang, X.; Dinh, C.-T.; Wang, Y.; Wang, Y.; Sinton, D.; Sargent, E. H. Hydroxide Promotes Carbon Dioxide Electroreduction to Ethanol on Copper via Tuning of Adsorbed Hydrogen. *Nat. Commun.* **2019**, *10*, 5814.
- (23) Ren, D.; Ang, B. S. H.; Yeo, B. S. Tuning the Selectivity of Carbon Dioxide Electrocatalysis toward Ethanol on Oxide-Derived Cu_xZn Catalysts. *ACS Catal.* **2016**, *6*, 8239–8247.
- (24) Morales-Guio, C. G.; Cave, E. R.; Nitopi, S. A.; Feaster, J. T.; Wang, L.; Kuhl, K. P.; Jackson, A.; Johnson, N. C.; Abram, D. N.; Hatsukade, T.; Hahn, C.; Jaramillo, T. F. Improved CO₂ Reduction Activity towards C₂₊ Alcohols on a Tandem Gold on Copper Electrocatalyst. *Nat. Catal.* **2018**, *1*, 764–771.
- (25) Ma, S.; Sadakiyo, M.; Heima, M.; Luo, R.; Haasch, R. T.; Gold, J. I.; Yamauchi, M.; Kenis, P. J. Electrocatalysis of Carbon Dioxide to Hydrocarbons Using Bimetallic Cu-Pd Catalysts with Different Mixing Patterns. *J. Am. Chem. Soc.* **2017**, *139*, 47–50.
- (26) Lee, S.; Park, G.; Lee, J. Importance of Ag-Cu Biphasic Boundaries for Selective Electrochemical Reduction of CO₂ to Ethanol. *ACS Catal.* **2017**, *7*, 8594–8604.
- (27) Liang, Z.-Q.; Zhuang, T.-T.; Seifitokaldani, A.; Li, J.; Huang, C.-W.; Tan, C.-S.; Li, Y.; De Luna, P.; Dinh, C. T.; Hu, Y.; Xiao, Q.; Hsieh, P.-L.; Wang, Y.; Li, F.; Quintero-Bermudez, R.; Zhou, Y.; Chen, P.; Pang, Y.; Lo, S.-C.; Chen, L.-J.; et al. Copper-on-Nitride Enhances the Stable Electrosynthesis of Multi-Carbon Products from CO₂. *Nat. Commun.* **2018**, *9*, 3828.
- (28) Shao, Q.; Wang, P.; Huang, X. Opportunities and Challenges of Interface Engineering in Bimetallic Nanostructure for Enhanced Electrocatalysis. *Adv. Funct. Mater.* **2019**, *29*, 1806419.
- (29) Wang, P.; Qiao, M.; Shao, Q.; Pi, Y.; Zhu, X.; Li, Y.; Huang, X. Phase and Structure Engineering of Copper-Tin Heterostructures for Efficient Electrochemical Carbon Dioxide Reduction. *Nat. Commun.* **2018**, *9*, 4933.
- (30) Rogers, C.; Perkins, W. S.; Veber, G.; Williams, T. E.; Cloke, R. R.; Fischer, F. R. Synergistic Enhancement of Electrocatalytic CO₂ Reduction with Gold Nanoparticles Embedded in Functional Graphene Nanoribbon Composite Electrodes. *J. Am. Chem. Soc.* **2017**, *139*, 4052–4061.
- (31) Subbaraman, R.; Tripkovic, D.; Strmcnik, D.; Chang, K.-C.; Uchimura, M.; Paulikas, A. P.; Stamenkovic, V.; Markovic, N. M. Enhancing Hydrogen Evolution Activity in Water Splitting by Tailoring Li⁺-Ni(OH)₂-Pt Interfaces. *Science* **2011**, *334*, 1256–1260.
- (32) Chong, L.; Wen, J.; Kubal, J.; Sen, F. G.; Zou, J.; Greeley, J.; Chan, M.; Barkholtz, H.; Ding, W.; Liu, D.-J. Ultralow-Loading Platinum-Cobalt Fuel Cell Catalysts Derived from Imidazolate Frameworks. *Science* **2018**, *362*, 1276–1281.
- (33) Kim, C.; Möller, T.; Schmidt, J.; Thomas, A.; Strasser, P. Suppression of Competing Reaction Channels by Pb D-datom Decoration of Catalytically Active Cu Surfaces during CO₂ Electroreduction. *ACS Catal.* **2019**, *9*, 1482–1488.
- (34) Garza, A. J.; Bell, A. T.; Head-Gordon, M. Mechanism of CO₂ Reduction at Copper Surfaces: Pathways to C₂ Products. *ACS Catal.* **2018**, *8*, 1490–1499.
- (35) Zheng, Y.; Vasileff, A.; Zhou, X.; Jiao, Y.; Jaroniec, M.; Qiao, S.-Z. Understanding the Roadmap for Electrochemical Reduction of CO₂ to Multi-Carbon Oxygenates and Hydrocarbons on Copper-Based Catalysts. *J. Am. Chem. Soc.* **2019**, *141*, 7646–7659.
- (36) Li, Q.; Fu, J.; Zhu, W.; Chen, Z.; Shen, B.; Wu, L.; Xi, Z.; Wang, T.; Lu, G.; Zhu, J.; Sun, S. Tuning Sn-Catalysis for Electrochemical Reduction of CO₂ to CO via the Core/Shell Cu/SnO₂ Structure. *J. Am. Chem. Soc.* **2017**, *139*, 4290–4293.
- (37) Yamaguchi, Y.; Shiota, M.; Nakayama, Y.; Hirai, N.; Hara, S. Combined *in Situ* EC-AFM and CV Measurement Study on Lead Electrode for Lead-Acid Batteries. *J. Power Sources* **2001**, *93*, 104–111.

- (38) Weekes, D. M.; Salvatore, D. A.; Reyes, A.; Huang, A.; Berlinguet, C. P. Electrolytic CO₂ Reduction in a Flow Cell. *Acc. Chem. Res.* **2018**, *51*, 910–918.
- (39) Zhuang, T.-T.; Liang, Z.-Q.; Seifitokaldani, A.; Li, Y.; De Luna, P.; Burdyny, T.; Che, F.; Meng, F.; Min, Y.; Quintero-Bermudez, R.; Dinh, C. T.; Pang, Y.; Zhong, M.; Zhang, B.; Li, Jun.; Chen, P.; Zheng, X.; Liang, H.; Ge, W.; Ye, B.; et al. Steering Post-C-C Coupling Selectivity Enables High Efficiency Electroreduction of Carbon Dioxide to Multi-Carbon Alcohols. *Nat. Catal.* **2018**, *1*, 421–428.
- (40) De Luna, P.; Quintero-Bermudez, R.; Dinh, C. T.; Ross, M. B.; Bushuyev, O. S.; Todorović, P.; Regier, T.; Kelley, S. O.; Yang, P.; Sargent, E. H. Catalyst Electro-Redeposition Controls Morphology and Oxidation State for Selective Carbon Dioxide Reduction. *Nat. Catal.* **2018**, *1*, 103–110.
- (41) Huang, C.; Wen, J.; Sun, Y.; Zhang, M.; Bao, Y.; Zhang, Y.; Liang, L.; Fu, M.; Wu, J.; Ye, D.; Chen, L. CO₂ Hydrogenation to Methanol over Cu/ZnO Plate Model Catalyst: Effects of Reducing Gas Induced Cu Nanoparticle Morphology. *Chem. Eng. J.* **2019**, *374*, 221–230.
- (42) Kondo, M.; Nakajima, Y.; Tanaka, T.; Nozawa, T.; Yokomine, T. Experimental Study on Chemical Behaviors of Non-Metal Impurities in Pb, Pb-Bi and Pb-Li by Temperature Programmed Desorption Mass Spectrometer Analysis. *Plasma & Fusion Res.* **2016**, *11*, 2405076.
- (43) Cheng, T.; Xiao, H.; Goddard, W. A., III Reaction Mechanisms for the Electrochemical Reduction of CO₂ to CO and Formate on the Cu(100) Surface at 298 K from Quantum Mechanics Free Energy Calculations with Explicit Water. *J. Am. Chem. Soc.* **2016**, *138*, 13802–13805.
- (44) Cheng, T.; Xiao, H.; Goddard, W. A., III Full Atomistic Reaction Mechanism with Kinetics for CO Reduction on Cu(100) from *ab Initio* Molecular Dynamics Free-Energy Calculations at 298 K. *Proc. Natl. Acad. Sci. U. S. A.* **2017**, *114*, 1795–1800.
- (45) Kresse, G.; Hafner, J. *Ab Initio* Molecular Dynamics for Liquid Metals. *Phys. Rev. B: Condens. Matter Mater. Phys.* **1993**, *47*, 558–561.
- (46) Kresse, G.; Hafner, J. *Ab Initio* Molecular-Dynamics Simulation of the Liquid-Metal-Amorphous-Semiconductor Transition in Germanium. *Phys. Rev. B: Condens. Matter Mater. Phys.* **1994**, *49*, 14251–14269.
- (47) Kresse, G.; Furthmüller, J. Efficient Iterative Schemes for *ab Initio* Total-Energy Calculations Using a Plane-Wave Basis Set. *Phys. Rev. B: Condens. Matter Mater. Phys.* **1996**, *54*, 11169–11186.
- (48) Kresse, G.; Furthmüller, J. Efficiency of *ab-Initio* Total Energy Calculations for Metals and Semiconductors Using a Plane-Wave Basis Set. *Comput. Mater. Sci.* **1996**, *6*, 15–50.
- (49) Perdew, J. P.; Chevary, J. A.; Vosko, S. H.; Jackson, K. A.; Pederson, M. R.; Singh, D. J.; Fiolhais, C. Atoms, Molecules, Solids, and Surfaces: Applications of the Generalized Gradient Approximation for Exchange and Correlation. *Phys. Rev. B: Condens. Matter Mater. Phys.* **1992**, *46*, 6671–6687.
- (50) Perdew, J. P.; Burke, K.; Ernzerhof, M. Generalized Gradient Approximation Made Simple. *Phys. Rev. Lett.* **1996**, *77*, 3865–3868.
- (51) Grimme, S.; Ehrlich, S.; Goerigk, L. Effect of the Damping Function in Dispersion Corrected Density Functional Theory. *J. Comput. Chem.* **2011**, *32*, 1456–1465.
- (52) Mathew, K.; Sundararaman, R.; Letchworth-Weaver, K.; Arias, T. A.; Hennig, R. G. Implicit Solvation Model for Density-Functional Study of Nanocrystal Surfaces and Reaction Pathways. *J. Chem. Phys.* **2014**, *140*, No. 084106.
- (53) Mathew, K.; Kolluru, V. S. C.; Mula, S.; Steinmann, S. N.; Hennig, R. G. Implicit Self-Consistent Electrolyte Model in Plane-Wave Density-Functional Theory. *J. Chem. Phys.* **2019**, *151*, 234101.